

AD/A-006 554

WIND WAVE STUDIES. PART 2. THE  
PARABOLIC ANTENNA AS A WAVE PROBE

Tyrone R. Larson, et al

Naval Research Laboratory  
Washington, D. C.

31 December 1974

DISTRIBUTED BY:

**NTIS**

National Technical Information Service  
U. S. DEPARTMENT OF COMMERCE

REPORT DOCUMENTATION PAGE		READ INSTRUCTIONS BEFORE COMPLETING FORM
1. REPORT NUMBER NRL Report 7850	2. GOVT ACCESSION NO.	3. RECIPIENT'S CATALOG NUMBER <b>AD/A-006554</b>
4. TITLE (and Subtitle) WIND WAVE STUDIES: PART 2-THE PARABOLIC ANTENNA OR A WAVE PROBE		5. TYPE OF REPORT & PERIOD COVERED
7. AUTHOR(s) Tyrone R. Larson John W. Wright		6. PERFORMING ORG. REPORT NUMBER
9. PERFORMING ORGANIZATION NAME AND ADDRESS Department of the Navy Office of Naval Research Arlington, VA 22217		8. CONTRACT OR GRANT NUMBER(s) NRL Problem RO7-17
11. CONTROLLING OFFICE NAME AND ADDRESS		10. PROGRAM ELEMENT (PROJECT, TASK AREA & WORK UNIT NUMBERS) WR021-01-002
14. MONITORING AGENCY NAME & ADDRESS (if different from Controlling Office)		12. REPORT DATE December 31, 1974
		13. NUMBER OF PAGES 23
		15. SECURITY CLASS. (of this report) UNCLASSIFIED
		15a. DECLASSIFICATION/DOWNGRADING SCHEDULE
16. DISTRIBUTION STATEMENT (of this Report)  Approved for public release; distribution unlimited.		
17. DISTRIBUTION STATEMENT (of the abstract entered in Block 20, if different from Report)		
18. SUPPLEMENTARY NOTES		
19. KEY WORDS (Continue on reverse side if necessary and identify by block number) Bragg scattering focussed parabola water wave probe  Reproduced by NATIONAL TECHNICAL INFORMATION SERVICE U.S. Department of Commerce Springfield, VA. 22151		
20. ABSTRACT (Continue on reverse side if necessary and identify by block number) Coherent microwave backscatter is the basis of a probe technique useful for studying surface water waves in a laboratory tank. A parabolic antenna is focussed to give a plane wave at short range, typically 1.2 m, and an illuminated area of controllable size. The technique strongly discriminates against all water waves except those which have a particular Bragg resonant wavelength ranging between 0.25 cm and 10 cm and propagate parallel to the plane of incidence. The resulting doppler spectra provide a powerful tool for wind wave, breaking, and spray studies. A unique method for directly measuring the water wavenumber resolution is described, together with a		

DD FORM 1 JAN 73 1473

EDITION OF 1 NOV 65 IS OBSOLETE  
S/N 0102-014-6601

SECURITY CLASSIFICATION OF THIS PAGE (When Data Entered)

technique for absolute calibration of the backscattered power in terms of wave height. As a consistency check on all the calibration procedures, the angular dependence and absolute value of the first-order scattering cross section from monochromatic water waves agrees with prediction.

## CONTENTS

INTRODUCTION .....	1
1. WAVE PROBE.....	1
2. DERIVATION OF THE FIELDS AT THE WATER SURFACE .....	5
3. PREDICTED PROBE RESPONSE .....	8
4. PROBE RESPONSE MEASUREMENTS .....	9
ACKNOWLEDGMENT .....	16
REFERENCES .....	16
APPENDIX—Calculation of Backscattered Power .....	17

## WIND WAVE STUDIES: PART 2--THE PARABOLIC ANTENNA AS A WAVE PROBE

### INTRODUCTION

A wave probe which uses microwave doppler backscatter has been developed and used for several years. The description given here is intended to make this technique for studying water waves more widely known and more accessible to other groups. The general technique of doppler backscatter is discussed in section 1, as are several unique advantages of the wave probe. Section 2 treats the illumination pattern from a focussed parabolic antenna, and section 3 treats the backscatter response of such an antenna. A first-order derivation of the scattering produced by a rough surface is described in the appendix. These treatments are intended to show how the illuminated area and the water wavenumber resolution can be selected by appropriate choice of antenna properties. A unique method of directly measuring wavenumber resolution is described in section 4; representative results are presented. Measured real-space antenna patterns give the illuminated area at the water surface, which is necessary for absolute calibration of the backscattered power in terms of wave height. Backscatter produced by a known monochromatic wave is compared absolutely with the return predicted by the first-order theory as a consistency check on all the calibration procedures described.

### 1. WAVE PROBE

Waves on an air/water interface can be directly studied using the microwave doppler backscatter technique because of the large microwave reflection coefficient at this interface [1]. Microwave radiation is focussed on the surface using a parabolic antenna at short range, where "short" will be defined later in this section. The radiation scattered directly back into the illuminating antenna, or backscatter, is carefully measured for both amplitude and doppler frequency shift. In other words, the backscattered signal is coherently detected using a portion of the transmitted signal as a local oscillator. The scattering geometry is illustrated in Fig. 1. Microwave scattering from small amplitude water waves is discussed in detail in the appendix.

For incidence angles  $\theta$  away from  $0^\circ$  and  $90^\circ$ , essentially all of the first-order backscattered power is produced by water waves which are traveling in the direction defined by the plane of incidence and which have a resonant wavelength given by the microwave wavelength  $\lambda_0$  and  $\theta$  [2]. More specifically, the waves contributing to first-order backscatter must satisfy the two-dimensional Bragg condition

---

Note: Manuscript submitted November 27, 1974.

$$k_x = 2k_0 \cos \theta \equiv k_B \quad (1)$$

and

$$k_y = 0. \quad (2)$$

A wavenumber  $k$  has the usual definition  $2\pi/\lambda_0$ , that is,  $k_0$  is given by  $2\pi/\lambda_0$ . The  $x$  direction lies in the plane of incidence, along the undisturbed surface, as indicated in Fig. 1. Equation (1) reduces to

$$\lambda_B = \frac{\lambda_0}{2 \cos \theta}. \quad (3)$$

The region in  $k$  space singled out for study is illustrated in Fig. 2, where resolution is indicated by  $\Delta k_x$  and  $\Delta k_y$ .

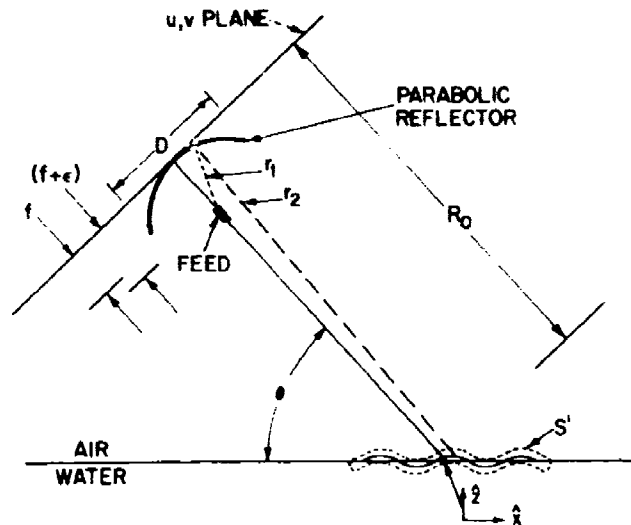


Fig. 1—Coordinate systems and geometry

This  $k$ -space selectivity is possible because the measurement is inherently area extensive. In a sense, one is using an infinite number of point probes spread in a dense array over the illuminated area. The field distribution over this area at the water surface, and hence the resolution about  $k = (k_B, 0)$ , is determined by antenna geometry. Different values of  $k_B$  can be chosen by varying  $\theta$  or  $\lambda_0$  or both. Our measurements extend from a water wavelength of 10 cm (4.30 GHz,  $70^\circ$ ) to 0.25 cm (70.1 GHz,  $30^\circ$ ). Spatial averaging over a section of tank width, common to point-probe techniques, is done automatically.

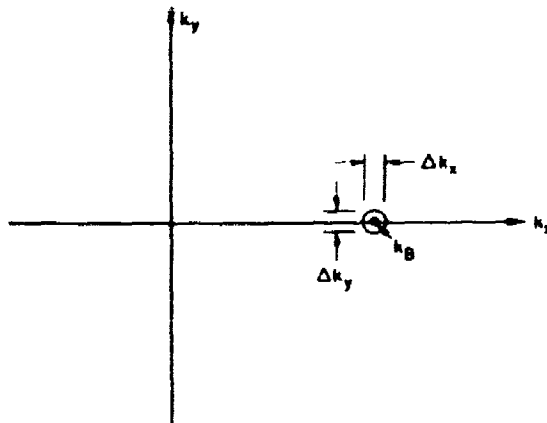


Fig. 2—Region in water wave  $k$  space about  $(k_B, 0)$  studied by this probe technique. Resolution  $\Delta k_x, \Delta k_y$  is discussed in the text.

The output of this wave probe, when run through an audio spectrum analyzer, gives the wave spectrum evaluated at  $(k_B, 0)$ ,  $\Psi(k_B, 0, \omega)$ . Here  $\omega$  is  $2\pi$  times the water wave frequency, and  $\Psi(k_x, k_y, \omega)$  is the Fourier transform of the surface-displacement covariance, as defined by Phillips [3]. This output is an instantaneous doppler spectrum and is usually averaged in time to give mean doppler spectra. The region in water wave  $(\omega, k_x)$  space probed is shown in Fig. 2b. This spectral information is available because the measurement is temporally extensive. Spectral resolution is limited by data acquisition time and ultimately by the antenna pattern.

To further clarify the concept of a doppler spectrum, consider the doppler shift produced by a mechanically generated, small amplitude, monochromatic wave. Refer to Fig. 1, with such a wave propagating through the illuminated area. Each point on the waveform surface has a velocity component  $v_d$  along the microwave line of sight:

$$v_d = v_p \cos \theta, \quad (4)$$

where  $v_p$  is the water wave phase velocity in laboratory coordinates. Note that the scattering occurs at the air/water interface, or waveform surface, and not from individual water "particles" or from some "packet" of waves. Thus in Eq. (4) the phase velocity is the correct quantity, not a particle orbital velocity or a wave group velocity. The microwave doppler frequency shift  $\Delta f$  relative to the incident microwave frequency  $f_0$  is

$$\frac{\Delta f}{f_0} = \frac{2v_d}{c} \quad (5)$$

where  $c$  is the speed of light. Using

$$\omega = v_p k, \quad (6)$$

which is true for all water waves, in Eq. (5) gives

$$\Delta f = f_{\text{water}} \quad (7)$$

The doppler frequency shift of a first-order Bragg resonant water wave is always the frequency of the water wave in the laboratory frame.

As part of the antenna response measurements to be discussed later, the doppler shift produced by a mechanically generated monochromatic wave was measured directly for several values of  $k_B$ . The results are given in Fig. 3. For these data,  $\lambda_0$  was held constant at 3.20 cm (9.375 GHz), and  $k_B$  was changed by varying  $\theta$  in  $5^\circ$  increments. In each case the water wave frequency giving maximum backscatter is plotted vs the frequency determined from  $k_B$  using the dispersion relation for infinitesimal water waves:

$$\omega^2 = \left( 980 \frac{\text{cm}}{\text{s}^2} \right) k + \left( 75 \frac{\text{cm}^3}{\text{s}^2} \right) k^3 \quad (8)$$

As seen in Fig. 3, agreement is good. The slight systematic deviation may be due to an inaccurate  $\theta$  calibration or to bore-sight error.

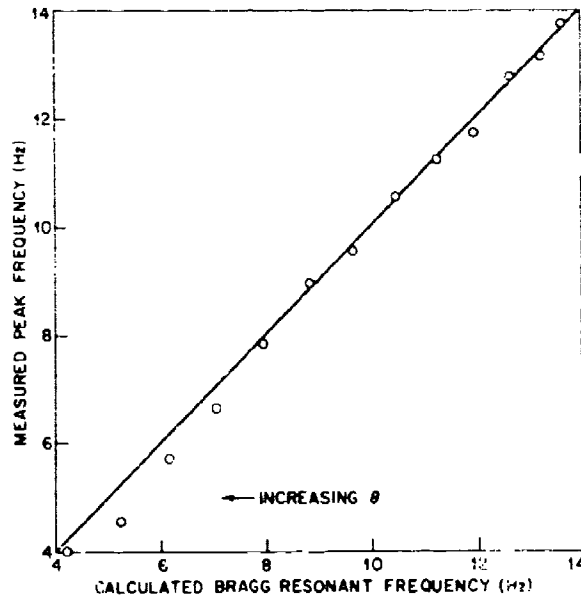


Fig. 3—Experimental verification of the fact that the doppler shift of a monochromatic Bragg resonant wave is given by the wave frequency. The measured doppler frequency is plotted vs the water wave frequency calculated from the known value of  $k_B$ .

Several other features of this wave probe should be mentioned. Dynamic range is limited by the audio-frequency signal-processing equipment. A range of  $10^3$  in wave height, or 60 dB in backscattered power, is readily achievable. Sensitivity is limited, in



practice, by how well the unshifted return from stationary room objects can be nulled on a microwave bridge. Surface displacements of  $10^{-2}$  mm are readily detectable, and linearity becomes a problem only for large-amplitude waves. Microwaves are "contactless." A slight heating is the only perturbation of the water surface produced, and this is usually negligible. Thus small waves can be accurately studied in the presence of longer and larger amplitude waves. Because water droplets scatter microwaves via 2 different mechanisms, wave breaking and the presence of spray can easily be detected [4]. Representative doppler spectra from wind-generated waves are shown in Fig. 4. The microwave wavelength is 7.00 cm and  $\theta$  is  $30^\circ$ . The air friction velocity  $\mu_a$  varies from 7 to 124 cm/s corresponding to wind speeds from 1.5 to 15 m/s. Interpretation of the complex features appearing at higher winds is beyond the scope of this report. Known sources of doppler bandwidth are finite scatterer lifetime, advection of scatterers by larger waves, and higher order scattering.

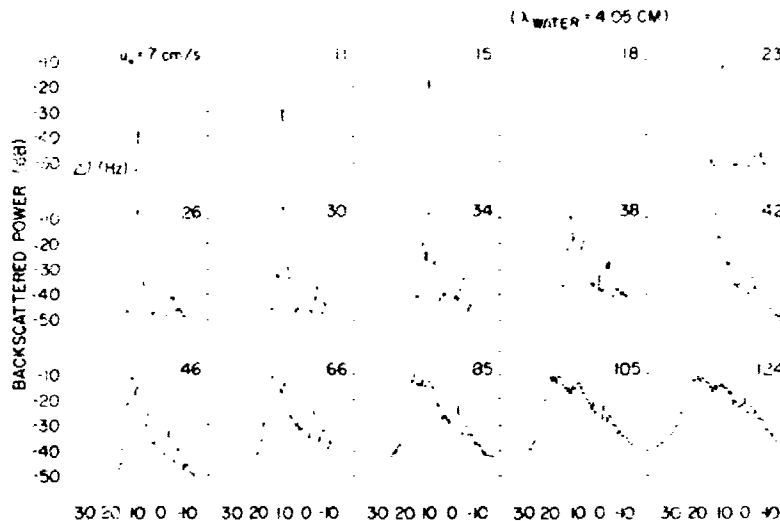


Fig. 4—Representative doppler spectra for several wind speeds. In each case,  $f_0 = 4.3$  GHz and  $\theta = 30^\circ$ .

## 2. DERIVATION OF THE FIELDS AT THE WATER SURFACE

Because of restrictions due to space, stability, convenience, and illuminated area, most laboratory wave-tank scattering measurements are made at ranges  $R_0$  within the Fresnel region. This region extends from several wavelengths from the antenna out to  $\approx 2D^2/\lambda_0$ , where  $D$  is the antenna diameter. The Fresnel region of a focussed parabolic antenna is particularly suited to laboratory scattering measurements. The microwave antenna pattern at  $R_0$  will be derived not for exact computation but to show its similarity to any other focussing system and to obtain important scaling parameters. Refer to Fig. 1 for the coordinate geometry.

Following Silver [5], the microwave field at a point  $(x, y)$  on the water surface can be written (suppressing an  $\exp(i\omega t)$  time dependence) as

$$E(x, y) = \frac{ik_0}{2\pi} \int_A F(u, v) (r_1 + r_2)^{-1} \exp[-ik_0(r_1 + r_2)] du dv. \quad (9)$$

Here  $F(u, v)$  is the antenna-feed field distribution over the aperture  $A$ . Expanding the phase term to second order in  $xR_0^{-1} \sin \theta$ ,  $yR_0^{-1}$ ,  $uR_0^{-1}$ , and  $vR_0^{-1}$  gives

$$\begin{aligned} r_1 + r_2 \approx & R_0 + f + \epsilon + x \cos \theta + \frac{1}{2} (u^2 + v^2) L(\epsilon) \\ & - uxR_0^{-1} \sin \theta - vyR_0^{-1} \\ & + x^2(2R_0)^{-1} \sin^2 \theta + y^2(2R_0)^{-1}, \end{aligned} \quad (10)$$

where higher order terms have been neglected. The coefficient of the  $u^2 + v^2$  term is

$$L(\epsilon) \equiv \frac{1}{R_0} + \frac{1}{f + \epsilon} - \frac{1}{f}, \quad (11)$$

where  $\epsilon$  is the spacing between the antenna feed and the "infinity" focal point of the parabola, as shown in Fig. 1. A focussed condition is defined by an  $\epsilon$  satisfying the lens equation

$$L(\epsilon) = 0. \quad (12)$$

To this order of approximation, phase variations at  $(x, y) = (0, 0)$  due to a finite aperture diameter can be "nulled" by a proper choice of  $\epsilon$ . The parabola can be effectively focussed on the water surface and can produce approximately plane waves over the illuminated area, even at short range.

Using Eq. (10) in the phase term of Eq. (9) and approximating the denominator by  $(R_0 + f)$  gives

$$\begin{aligned} E(x, y) = & \frac{ik_0}{2\pi(R_0 + f)} \exp \left[ -ik_0 \left( R_0 + f + \epsilon + x \cos \theta + \frac{x^2 \sin^2 \theta}{2R_0} + \frac{y^2}{2R_0} \right) \right] \\ & \times \int_{-\infty}^{\infty} F_1(u) \exp \left[ -ik_0 \left( \frac{ux \sin \theta}{R_0} + \frac{u^2 L(\epsilon)}{2} \right) \right] du \\ & \times \int_{-\infty}^{\infty} F_2(v) \exp \left[ -ik_0 \left( \frac{vy}{R_0} + \frac{v^2 L(\epsilon)}{2} \right) \right] dv. \end{aligned} \quad (13)$$

The feed gain function  $F(u, v)$  has been written as  $F_1(u)F_2(v)$  and defined as  $F_1 = F_2 = 0$  outside of the antenna aperture, which is adequate for this discussion. Both integrals in Eq. (13) are a Fourier transform of a product of two functions, that is, a convolution of two Fourier transforms. The coordinate transform pairs are  $u, \alpha x \sin \theta$  and  $v, \alpha y$ , where  $\alpha \equiv k_0/R_0$ . Denoting a Fourier transform by  $\cdot$  and a convolution by  $*$ ,

Eq. (13) becomes

$$E(x, y) = C_0 \exp(-ik_0 x \cos \theta) f_1(x) f_2(y), \quad (14)$$

where

$$C_0 = \frac{ik_0}{2\pi(R_0 + f)} \exp[ik_0(R_0 + f + \epsilon)], \quad (15)$$

$$f_1(x) = \exp\left(-i\frac{\alpha}{2}x^2 \sin^2 \theta\right) \left[ \hat{F}_1(\alpha x \sin \theta) + \exp\left(\frac{i\alpha^2 x^2 \sin^2 \theta}{k_0 L(\epsilon)}\right) \right], \quad (16)$$

and

$$f_2(y) = \exp\left(-i\frac{\alpha}{2}y^2\right) \left[ \hat{F}_2(\alpha y) + \exp\left(\frac{i\alpha^2 y^2}{k_0 L(\epsilon)}\right) \right]. \quad (17)$$

Exact calculation of the fields is tedious and requires the feed gain function to be specified. The direct-measurement techniques discussed in section 4 are more practical and more accurate. The important qualitative feature is that for  $L(\epsilon) = 0$ , the antenna pattern  $E(x, y)$  becomes approximately the Fourier transform of the feed gain function, scaled by  $\alpha \sin \theta$  or  $\alpha$ . Estimates of the minimum real-space pattern widths, in both direction, are

$$\Delta x \approx \frac{1}{\alpha \sin \theta \Delta u} \approx \frac{R_0 \lambda_0}{2\pi D \sin \theta} \quad (18)$$

and

$$\Delta y \approx \frac{1}{\alpha \Delta v} \approx \frac{R_0 \lambda_0}{2\pi D}. \quad (19)$$

Here  $\Delta u$  and  $\Delta v$  are the widths of  $F_1(u)$  and  $F_2(v)$  respectively and are approximated by  $D$ . In practice, most feeds have a gain function tapered from the center to edge of the parabola. This reduces  $\Delta u$  and  $\Delta v$  but improves the sidelobes. Other choices of  $\epsilon$  further broaden the real-space pattern. The pattern width in each direction in this case can be estimated using

$$(\Delta x)^2 \approx \left(\frac{R_0}{k_0 \sin \theta}\right)^2 \left[ \frac{1}{(\Delta u)^2} + \frac{L^2(\epsilon)}{4} \right] \quad (20)$$

and

$$(\Delta y)^2 \approx \left(\frac{R_0}{k_0}\right)^2 \left[ \frac{1}{(\Delta v)^2} + \frac{L^2(\epsilon)}{4} \right]. \quad (21)$$

From another viewpoint, the radius of the first Fresnel zone centered on the "spot" illuminated at the water surface is given by

$$r_F = \sqrt{\frac{\pi}{\alpha}} \approx \sqrt{\lambda_0 R_0}. \quad (22)$$

Taking the ratio

$$\frac{\Delta x}{r_F} \approx \frac{\sqrt{\lambda R_0}}{\Delta u} \approx \frac{\sqrt{\lambda R_0}}{D}$$

reveals that for sufficiently short ranges this first Fresnel zone is under-illuminated. In this sense one has an incident plane wave, and the illuminating patterns are transforms, as discussed previously.

### 3. PREDICTED PROBE RESPONSE

The successful use of this wave probe depends on understanding the effects of the illumination pattern on the backscattered power. Besides illuminated area, important factors are resolution in water wavenumber space, and absolute calibration in terms of wave height. For cases when the antenna pattern is important, the backscattered power is best calculated using an iterative integral method [6] which is particularly simple in first order. This is done in detail in the appendix. The first-order returned power is proportional, as described in the appendix, to a dimensionless cross section, or cross section per unit illuminated area:

$$\sigma_0 = 16\pi k_0^4 |g(\theta)|^2 \Psi(k_x, k_y, \omega) * V(k_x, k_y) \Big|_{\mathbf{k} = (k_B, 0)} \quad (24)$$

The transfer coefficient  $|g(\theta)|^2$  depends on the polarization and on the incidence angle. It is given in the appendix and is plotted by Wright [7]. The water wave spectrum to be measured,  $\Psi(k_B, 0, \omega)$ , is convolved with an antenna response function  $V(k_B, 0)$  which is normalized:

$$\int_{-\infty}^{\infty} V(k_x, k_y) dk_x dk_y = 1. \quad (25)$$

This function determines the resolution,  $\Delta k_x$  and  $\Delta k_y$ , possible about  $\mathbf{k} = (k_B, 0)$ . An interesting feature is that  $V(k_x, k_y)$  is related to the spatial Fourier transform of the antenna pattern at the water surface and thus to the feed gain function. More explicitly,

$$V(k_x, k_y) = \eta(k_x, k_y) * \eta(k_x, k_y), \quad (26)$$

where

$$\eta(k_x, k_y) \propto F\left(\frac{k_x}{\alpha \sin \theta}, \frac{k_y}{\alpha}\right). \quad (27)$$

This inverse-transform relationship between feed gain function, antenna pattern, and  $k$ -space response is typical of focussing systems. The scale factors in Eq. (27) allow one to predict resolutions for other sets of parameters  $D$ ,  $\theta$ ,  $k_0$ , and  $R_0$ , given one result initially.

The choice of antenna and range usually involves a compromise. If a large antenna diameter and short range are chosen to give severe underillumination and a good plane wave, the focussed spot may be only a Bragg wavelength or less in diameter and yield poor resolution in wavenumber. If overillumination is chosen, the Fresnel terms will produce sidelobes in  $V(k_x, k_y)$  and broaden the main lobe. For the antennas we have investigated, maximum resolution in wavenumber occurs near the  $L(\epsilon) = 0$  condition. It is practical, however, to enlarge the illuminated area by limited defocussing.

In any case, exact calculation of  $V(k_x, k_y)$  is complex and depends critically on the phase as well as on the amplitude of the fields produced by the antenna feed. It is much simpler and more accurate to measure  $V(k_x, k_y)$  directly using monochromatic, mechanically generated water waves. In this case the wave spectrum is narrow compared to  $V(k_x, k_y)$ . If the backscattered power is measured while the wave frequency (or  $k_x$ ) is slowly scanned,  $V[k(\omega), 0]$  is traced out. Although the cross section is not independent of range and antenna properties, it is given by

$$\sigma(\omega) = 8\pi k_0^4 h^2 |g^2(\theta)| V[k(\omega), 0] A_0, \quad (28)$$

where  $h$  is the mechanical-wave rms amplitude and  $A_0$  is the illuminated area, as defined in the appendix. To make this measurement, it is only necessary to keep  $h$  constant; the magnitude of  $V$  is obtained from the normalization condition, Eq. (25).

#### 4. PROBE RESPONSE MEASUREMENTS

The  $k$ -space response of this probe, or  $V[k(\omega), 0]$ , is measured by a technique which we believe has not been previously reported. With an antenna mounted above the water as in Fig. 1, monochromatic, mechanically generated water waves are propagated in the  $x$  direction through the illuminated area. The backscattered power, doppler shifted at the water wave frequency  $\omega_w$ , is plotted as a function of  $\omega_w$ , which is linearly swept. A sketch of the loudspeaker-driven mechanical wavemaker is shown in Fig. 5. A linear voltage ramp drives a voltage-controlled audio oscillator whose output is fed to the speaker after amplification. A few experimental pitfalls should be mentioned. The dimension  $b$  in Fig. 5 must be chosen to avoid mechanical resonances in the driven water column, especially near a Bragg frequency. An excessive insertion depth  $\alpha$  severely reduces amplitude output. At frequencies near 8 Hz, amplitude fluctuations are produced which vary slowly over several minutes. These are perhaps due to a resonant wave-wave interaction mechanism [8].

A representative trace of backscattered power vs water wave frequency  $f_w$  is shown in Fig. 6. For this example, these parameters apply:  $VV$  polarization,  $D = 30.5$  cm,  $R_0 = 1.22$  m,  $f_0 = 9.375$  GHz,  $\theta = 35^\circ$ , and  $\lambda_B = 1.95$  cm. The pattern shape is near gaussian, or parabolic when plotted logarithmically (Fig. 6). This gives very steep filter skirts indeed and makes the technique useful as a wave probe. Frequency resolution

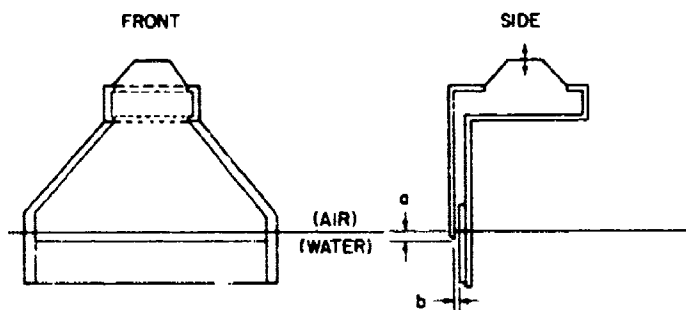


Fig. 5—Mechanical wave generator driven by a loudspeaker.

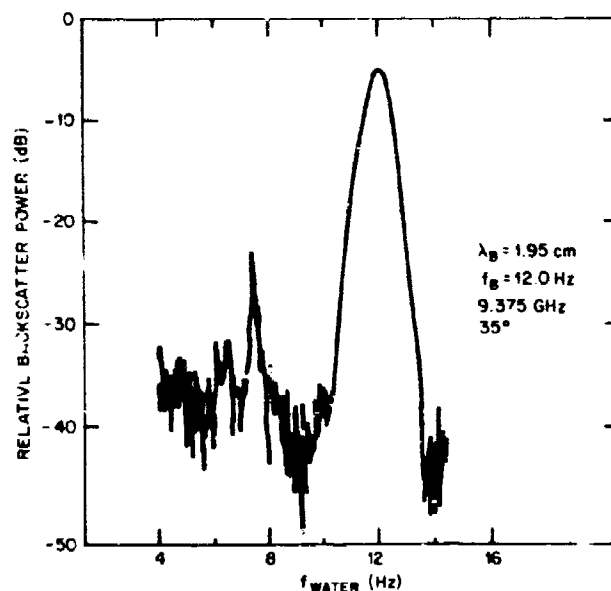


Fig. 6—Representative trace of backscattered power vs. the frequency of a monochromatic water wave propagating through the illuminated area. Note the sharp drop in response on either side of the Bragg resonant frequency.

$\Delta f_W$  can be read directly (for example, using a full width at 6 dB below maximum criterion). Wavenumber resolution is obtained from

$$\Delta k_x = \Delta \omega_W \left[ \frac{\partial \omega(k_B)}{\partial k} \right]^{-1}, \quad (29)$$

where  $\partial \omega(k_B)/\partial k$  is evaluated using Eq. (8). Structure appearing in the trace at  $f < f_B$  is probably caused by nonsinusoidal waveforms. A low-frequency wave could have a spatial harmonic at  $k_B$ . This trace is one of a series taken under identical conditions, except that  $\theta$  was varied in  $5^\circ$  increments for each trace. As discussed in section 1, the measured peak values of  $\omega_W$  are plotted in Fig. 3 vs the Bragg resonant frequencies predicted using Eqs. (1) and (8). The peak value of  $V(k_x, k_y)$  should be inversely proportional to the illuminated area, which in turn varies as  $\sin \theta$ . This is verified in Fig. 7 where the integrated area under the main peak of each trace is plotted vs  $\sin \theta$ . A straight-line dependence is verified. As  $\theta$  approaches  $90^\circ$ , interference from the large specularly reflected beam becomes severe. Thus the data have more scatter for these angles.

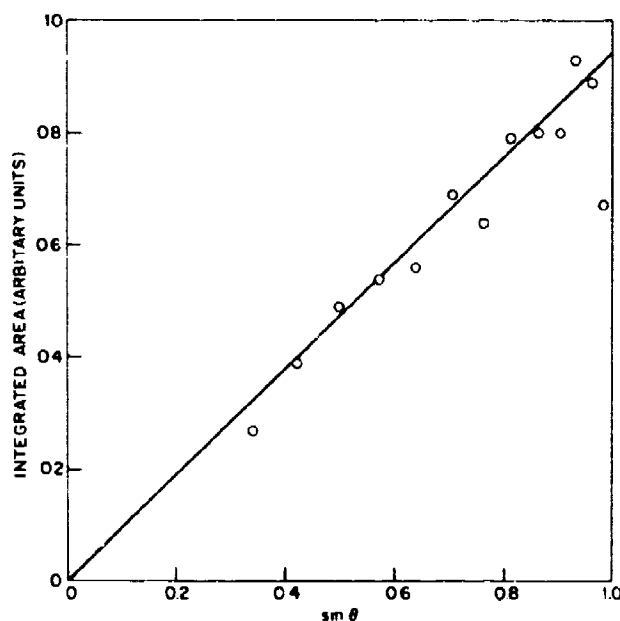


Fig. 7—Area under a series of antenna response curves like the one in Fig. 6, vs  $\sin \theta$ . Resolution scales inversely with the length of the illuminated area and directly with  $\sin \theta$ .

By taking traces at various antenna-feed positions, the dependence of  $k$ -space resolution on  $\epsilon$  can be investigated. Results of two series of traces are given in Fig. 8 and 9. Parameters for Fig. 8 are  $f_0 = 4.30$  GHz,  $D = 61$  cm,  $\theta = 60^\circ$ ,  $\lambda_B = 7.00$  cm, and a focal length of 20.3 cm; for Fig. 9,  $f_0 = 9.375$  GHz,  $D = 30.5$  cm,  $\theta = 45^\circ$ ,  $\lambda_B = 2.26$  cm, and a focal length of 10.2 cm. Both cases had the same range  $R_0$  of 1.22 m. For both

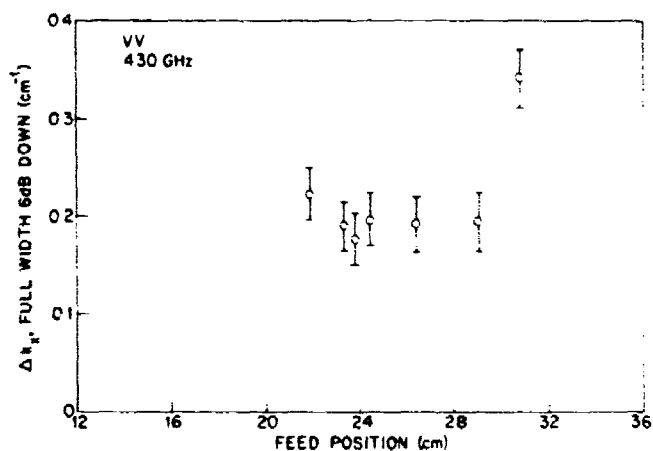


Fig. 8—Resolution  $\Delta k_x$  vs feed position (arbitrary origin) for  $\theta = 60^\circ$ ,  $D = 61$  cm,  $\lambda_B = 7.00$  cm,  $R_0 = 1.2$  m, and a focal length of 20.3 cm.

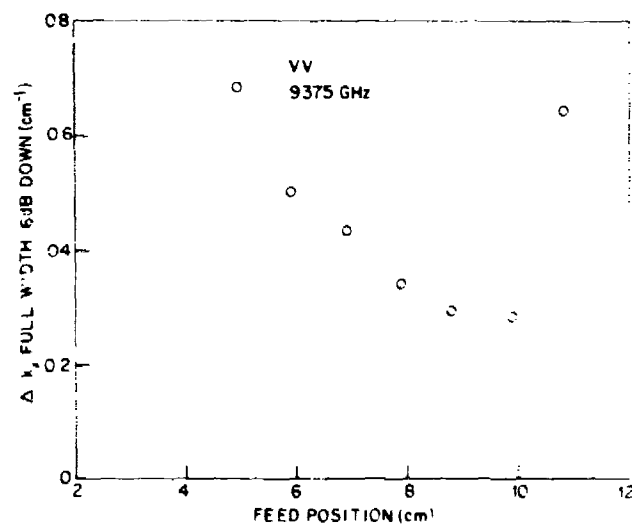


Fig. 9—Resolution  $\Delta k_x$  vs feed position (arbitrary origin) for  $\theta = 45^\circ$ ,  $D = 30.5$  cm,  $\lambda_B = 2.26$  cm,  $R_0 = 1.2$  m, and a focal length of 10.2 cm.



figures the wavenumber resolution obtained from Eq. (29) is plotted vs feed position in cm. The criterion for  $\Delta\omega_p$  is full width at 6 dB below maximum. The abscissa in each case has an arbitrary origin because for each feed the effective ray origin position is not known. The polarizations used are indicated. In both cases a range of  $\pm 15\%$  in  $\epsilon$  about the focussed position is available for varying the illuminated area, without severely degrading the resolution. The best wavenumber resolution from the data given here is  $\Delta k_x/k_B = 10\%$  for Fig. 9 and  $\Delta k_x/k_B = 20\%$  for Fig. 8.

Several real-space antenna patterns were measured to check their dependence on  $\epsilon$  and  $R_0$  and to determine the illuminated area  $A_0$ , defined by Eq. (46). These two-way patterns are measured by vertically lowering a metal sphere of known cross section [9a] through the radiated antenna field, with the axis of symmetry of the antenna horizontal. The range  $R_0$  was 1.22 m. The diameter of the metal sphere was typically  $\sim \lambda_0$ . Care in boresighting, or aligning the sphere to pass through the center of the pattern, is necessary since the main beam direction can deviate from the apparent antenna axis of symmetry by a few degrees. Pattern widths in the  $E$  and  $H$  planes are plotted vs feed position in Fig. 10 for the 30.5-cm parabola with focal length 10.2 cm at 9.375 GHz. Thus each plotted point is obtained from a measured pattern whose width is taken as the full pattern width at 6 dB below maximum. Figure 11 gives the same measurements for a 61-cm parabola with focal length 20.3 cm at 4.30 GHz. In both cases the shape of the plotted data has a broad minimum defining the focussed position. Because of the near-gaussian patterns, the illuminated area is proportioned to the product of these two widths. As a check on depth of field, Fig. 12 shows the  $E$ -plane main-lobe width vs  $R_0$  for the 4.30 GHz case. The feed position  $\epsilon$  was chosen to give a focus at a range of 1.5 m in this case. The pattern width scales linearly with  $R_0$ , as predicted by Eq. (18). The depth of field is thus adequate for most water wave measurements made in a laboratory tank. Illuminated area at any  $\theta$  can be obtained from the measured  $90^\circ$  values by dividing by  $\sin \theta$ . The pattern did not deteriorate drastically either in main-lobe shape or in sidelobe level for at least a  $\pm 15\%$  range in  $\epsilon/f$  about the focus for all frequencies and parabolas used. Thus changing illuminated area by focussing a parabola in the near field is a viable procedure. By comparing real-space pattern widths for the  $E$  and  $H$  planes, the resolution  $\Delta k_y$  can be obtained from  $\Delta k_x$ .

Finally, as a consistency check on all of the calibration measurements made using this probe, returned power scattered from a monochromatic mechanically generated wave at  $k = k_B$  was measured absolutely at several angles; these measurements are compared in the appendix with the results of the first-order scattering theory. The data are taken from the same series of 9.375-GHz traces taken at  $5^\circ$  increments in  $\theta$  previously discussed. The quantities  $A_0$ ,  $V(k_B, 0)$ , and  $h$  were measured independently for each angle and used in Eqs. (28), (43), (44), and (45) to predict  $P_r/P_t$  vs  $\theta$ . These predicted values are compared to actual measured values of  $P_r/P_t$  in Fig. 13, where both are plotted vs  $\theta$ . The measured returned power is compared in each case to a standard reflection. This in turn is calibrated with the return from a metal sphere at a known range and focus setting. The measured  $k$ -space patterns, together with the normalization condition, Eq. (25), give the  $V(k_B, 0)$  term. The water wave amplitude  $h$  was measured in each case by photographing the image of an illuminated slit reflected in the water surface. Both measured and calculated values of  $P_r/P_t$  are normalized to a water wave amplitude of 0.27 mm, peak to peak. Actual amplitude was kept within a factor of two of this value for each case. The value of

$$\delta \equiv k_B h \sin \theta \equiv 2k_0 h \sin \theta \quad (30)$$

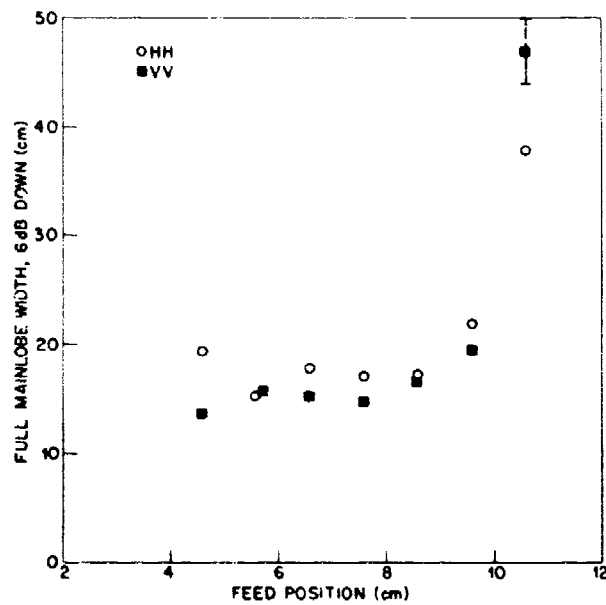


Fig. 10—Real-space antenna pattern width vs feed position (same origin as that of Fig. 9).  $D = 30.5$  cm,  $f_0 = 9.375$  GHz, focal length = 10.2 cm, and  $R_0 = 1.2$  m. Both polarization directions are given, as indicated.

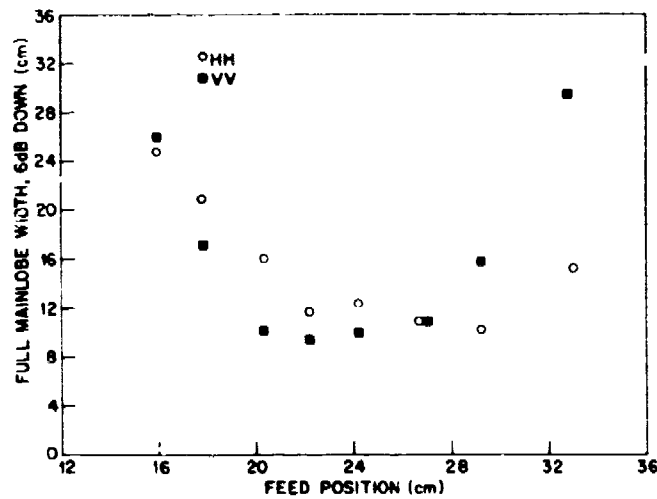


Fig. 11—Real-space antenna pattern width vs. feed position (same origin as Fig. 8).  $D = 61$  cm, focal length = 20.3 cm,  $f_0 = 4.30$  GHz, and  $R_0 = 1.2$  m. Both polarization directions are given, as indicated.

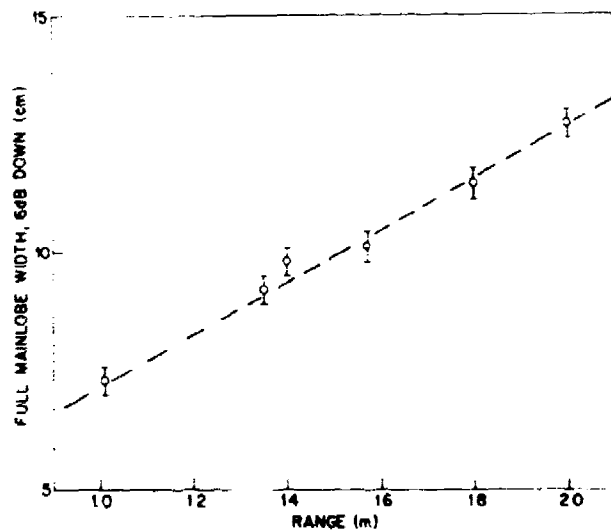


Fig. 12—Pattern width vs range  $R_0$  for a fixed feed position.  $D = 61$  cm, focal length = 20.3 cm, and  $f_0 = 4.30$  GHz.

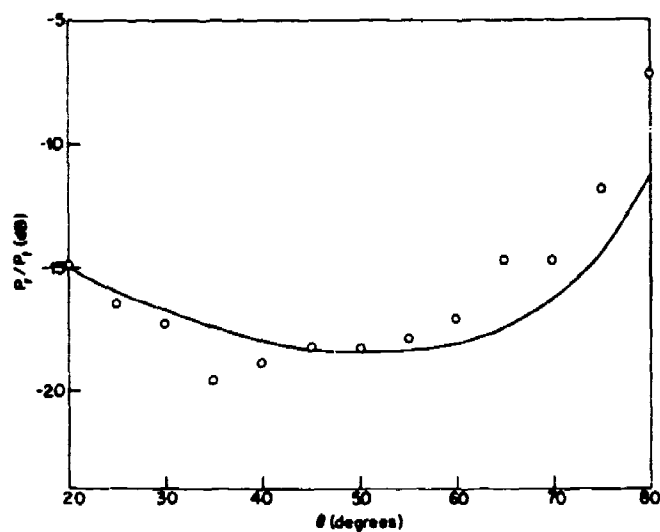


Fig. 13—Measured values of backscattered power vs  $\theta$ . The solid line gives the values predicted by the first-order scattering theory in the appendix.

has a maximum of 0.06. Thus the Rayleigh criterion,  $\delta < 1$ , was certainly satisfied, and first-order scattering theory should be sufficiently accurate. Water wave attenuation is measured directly by using two illuminated slits. If care is taken to blow off contaminant surface films, attenuation is small enough to be neglected over the length of the illuminated area. This area  $A_0$  is obtained from real-space patterns, as described previously. The transfer coefficient  $|g(\theta)|^2$  is calculated using  $55(1 - i0.55)$  for the relative dielectric constant of water. Agreement is satisfactory. At the angles nearer normal incidence, interference from the specularly scattered beam probably caused the measured values to be slightly high. However, the results of first-order scattering theory are certainly born out, and the calibration procedures described in this report are consistent.

#### ACKNOWLEDGMENT

Much of the 9.375 GHz data were taken by J.R. Duncan whose aid is gratefully acknowledged.

#### REFERENCES

1. J.P. Hollinger, "Microwave Properties of a Calm Sea," NKL Branch Report 7110-2, Aug. 15, 1973, AD 771374.
2. J.W. Wright and W.C. Keller, "Doppler Spectra in Microwave Scattering from Wind Waves," *Phys. Fluids* 14, 466 (1971).
3. O.M. Phillips, *The Dynamics of the Upper Ocean*, Cambridge University Press, 1969, Chapter 4, p. 75.
4. J.W. Wright, J.R. Duncan, and W.C. Keller, "Wind Wave Studies, Part 1—Doppler Spectra," NRL Report 7473, Nov. 8, 1972.
5. S. Silver, editor, *Microwave Antenna Theory and Design*, M.I.T. Radiation Laboratory Series Vol. 12, McGraw-Hill, Chapter 6, p. 170.
6. J.W. Wright, "Backscattering from Capillary Waves with Applications to Sea Clutter," *IEEE Trans., Antennas and Propagation* AP-14, 749 (1966).
7. J.W. Wright, "A New Model for Sea Clutter," *IEEE Trans., Antennas and Propagation* AP-16, 217 (1968).
8. L.F. McGoldrick, "An Experiment on Second-Order Capillary Gravity Resonant Wave Interactions," *J. Fluid Mech.* 40, 251 (1970).
9. D.E. Kerr, editor, *Propagation of Short Radio Waves*, M.I.T. Radiation Laboratory Series Vol. 13, McGraw-Hill, New York, 1951:
  - a. p. 453
  - b. p. 693

## APPENDIX

### CALCULATION OF BACKSCATTERED POWER

In this case where the antenna pattern is important, the backscattered power is best calculated using an iterative integral method which is particularly simple in first order [7]. Referring to Fig. 1, the resultant total field in all space is denoted by  $E_0, H_0$  for an unperturbed water surface. When the surface is now perturbed by a displacement  $\gamma(x, y, t)$ , assume that the resultant total field in all space can be written:

$$E = E_0 + e_1 + e_2 + \dots; \quad (31a)$$

$$H = H_0 + h_1 + h_2 + \dots \quad (31b)$$

Successive terms are proportional to ascending powers of a dimensionless expansion parameter proportional to surface displacement, for example, the  $\delta$  defined in Eq. (30). Using a general scattering theorem [9b], the average power backscattered by the rough surface  $\gamma(x, y, t)$  is

$$P_r = \frac{1}{16P_t^2} \left| \oint_{s'} (E \times H_0 - E_0 \times H) \cdot n \, ds' \right|^2, \quad (32)$$

where  $P_t$  is the transmitted power. Here  $n$  is the local surface normal, and  $s'$  is a surface of integration enclosing  $\gamma(x, y, t)$  above and below, as shown in Fig. 1. Kerr's method is readily adapted to calculation of the received power spectral density or doppler spectrum  $D(\omega)$

$$\begin{aligned} \frac{D(\omega)}{P_t} &= \lim_{T \rightarrow \infty} \frac{1}{32\pi T P_t^2} \left| \int_{-T/2}^{T/2} e^{i\omega t} dt \right. \\ &\quad \times \left. \int_{s=\gamma(x,y,t)} [(n \times E) \cdot \Delta H_0 + (n \times H) \cdot \Delta E_0] \, ds \right|^2, \end{aligned} \quad (33)$$

where  $\Delta E_0, \Delta H_0$  are the discontinuities in the unperturbed field across the perturbed surface  $\gamma(x, y, t)$  and  $n$  is the normal to the perturbed surface.

$$\begin{aligned} \Delta E_0 &= (E_0^{\text{air}} - E_0^{\text{water}}) \Big|_{z=0} \\ &\quad + \left( \frac{\partial E_0^{\text{air}}}{\partial z} - \frac{\partial E_0^{\text{water}}}{\partial z} \right) \Big|_{z=0} \gamma(x, y, t) + \dots \end{aligned} \quad (34)$$

and similarly for  $\Delta H_0$ . Neglected in Eq. (33) were terms of order  $(\Delta\omega/\omega_0)^2 P_t$ , where  $\Delta\omega$  is the width of the doppler spectrum and  $\omega_0$  is the microwave frequency. The finite antenna pattern assures negligible contribution to the spatial integral at large distances. The total backscattered power is

$$P_r = \int_{-\infty}^{\infty} D(\omega) d\omega. \quad (35)$$

The zero-order fields at the surface are obtained in principle from Eq. (14). However, these fields can be assumed locally plane for the purpose of computing  $\Delta E_0$  and  $\Delta H_0$ . That is, the relationships between electric and magnetic fields and their derivatives are assumed to be those for plane waves. This may introduce errors in the received power of magnitude  $(D/R_c)^2$ .

Substituting Eq. (34) in Eq. (33) reveals the advantage of this calculation technique:  $a_1$ ,  $h_1$ , and higher order terms are not needed to evaluate the integral to first order. Equation (33) becomes

$$\begin{aligned} \frac{D(\omega)}{P_t} &= \lim_{T \rightarrow \infty} \frac{(4k_0)^2}{2\pi T} \left| g(\theta) \int_{-T/2}^{T/2} e^{i\omega t} dt \right. \\ &\quad \times \left. \iint_{-\infty}^{\infty} \gamma(x, y, t) \frac{E_i H_i}{2P_t} e^{-ik_B x} dx dy \right|^2, \end{aligned} \quad (36)$$

where  $k_B$  is  $2k_0 \cos \theta$ . The product  $E_i(x, y)H_i(x, y)/2$  is the complex illumination pattern, where  $H_i = E_i/Z_0$ , with  $Z_0$  the characteristic impedance of free space. Thus  $|E_i(0, 0)H_i(0, 0)|/2$  is the mean incident intensity at the center of the illuminated area. The angular dependence is given by

$$|g(\theta)|_{VV}^2 = \left| \frac{2\omega_0^2}{c^2} \sin^2 \theta \frac{(1 - \epsilon') [\epsilon' (1 + \cos^2 \theta) - \cos^2 \theta]}{[\epsilon' \sin^2 \theta + (\epsilon' - \cos^2 \theta)^{1/2}]^2} \right|^2 \quad (37)$$

and

$$|g(\theta)|_{HH}^2 = \left| \frac{2\omega_0^2}{c^2} \sin^2 \theta \frac{(1 - \epsilon')}{[\sin \theta + (\epsilon' - \cos^2 \theta)]^2} \right|^2, \quad (38)$$

where  $\epsilon'$  is the dielectric constant of water. The subscripts define the  $E$ -field polarization; for example,  $VV$  implies polarization which is vertical, or in the plane of incidence, for both transmit and receive. Note that in actual CW doppler measurements, an audio-frequency offset is introduced to prevent folding positive and negative velocities onto one another in the detection process. This offset has been omitted here.

As in most scattering problems, it is useful to introduce the scattering cross section  $\sigma$ , which is defined by the radar range equation

$$\frac{P_r}{P_t} = \frac{G^2 \sigma \lambda_0^2}{(4\pi)^3 R_0^4} \quad (39)$$

Again, by definition the antenna gain  $G$  is

$$G = 4\pi R_0^2 \frac{|E(R_0)H(R_0)|}{2P_t}, \quad (40)$$

and Eq. (40) can be rewritten

$$\frac{P_r}{P_t} = \frac{1}{4} |E(R_0)H(R_0)|^2 \frac{\pi \sigma}{P_t^2 k_0^2} \quad (41)$$

The definition of  $\sigma$  based on Eq. (39) is valid in the far-field limit  $R_0 \gg D^2/\lambda_0$ . It is only then (and in the geometrical-optics limit) that  $\sigma$  is truly independent of range and antenna properties. For our case, however, we substitute Eq. (41) in Eq. (36) and replace  $E(R_0)H(R_0)$  by  $E_i(0, 0)H(0, 0)$ . This gives a definition of  $\sigma$  applicable for this near-field, doppler-radar case:

$$\sigma(\omega) = \lim_{T \rightarrow \infty} \frac{(2k_0)^4}{8\pi^2 T} \left| g(\theta) \int_{-T/2}^{T/2} e^{-i\omega t} dt \right. \\ \left. \times \iint_{-\infty}^{\infty} \gamma(x, y, t) \frac{E_i(x, y)H_i(x, y)}{E_i(0, 0)H_i(0, 0)} e^{-ik_B x} dx dy \right|^2, \quad (42)$$

where

$$\sigma = \int_{-\infty}^{\infty} \sigma(\omega) d\omega. \quad (43)$$

The definition of  $\sigma$  is extremely useful because the simplest way to calibrate received power in these measurements is to compare it with the backscattered power from a target of theoretically known cross section, usually a small metal sphere. The theoretical cross section is computed from a boundary-value problem, assuming incident plane waves. As this is consistent with our assumptions, no further approximation is made when using this calibration procedure. To summarize, by comparing the backscattered power from the rough surface with that from a highly conducting sphere placed at the center of illumination, we can obtain a cross section (in  $\text{cm}^2$ , say) for the rough surface.

If  $\gamma(x, y, t)$  is a random surface for which a suitable ensemble can be constructed, a dimensionless cross section  $\sigma_0$  can be defined:

$$\sigma_0 = \frac{\sigma}{A_0}, \quad (44)$$

where

$$A_0 = \iint \left| \frac{E_i(x, y) H_i(x, y)}{E_i(0, 0) H_i(0, 0)} \right|^2 dx dy. \quad (45)$$

Thus  $\sigma_0$  is a dimensionless cross section normalized by the illuminated area defined by Eq. (45) and is independent of range and antenna properties in many practical cases. To compute  $\sigma_0$ , we use the identity

$$\begin{aligned} \left| \iiint f(x, y, t) dx dy dt \right|^2 &\equiv \iiint \iiint f(x, y, t) \\ &\quad \times f(x + \Lambda_x, y + \Lambda_y, t + \tau) \\ &\quad \times dx dy dt d\Lambda_x d\Lambda_y d\tau \end{aligned} \quad (46)$$

and take an ensemble average of Eq. (42). The result is

$$\begin{aligned} \sigma_0(\omega) &= \frac{(2k_0)^4}{8\pi^2} |\zeta(\theta)|^2 \iiint Z(\Lambda_x, \Lambda_y, \tau) R(\Lambda_x, \Lambda_y) \\ &\quad \times e^{ik_B \Lambda_x} e^{i\omega \tau} d\Lambda_x d\Lambda_y d\tau, \end{aligned} \quad (47)$$

where  $Z(\Lambda_x, \Lambda_y, \tau)$  is the surface covariance

$$Z(\Lambda_x, \Lambda_y, \tau) \equiv \langle \gamma(x, y, t) \gamma(x + \Lambda_x, y + \Lambda_y, t + \tau) \rangle, \quad (48)$$

$$R(\Lambda_x, \Lambda_y) \equiv \frac{1}{A_0} \iint U(x, y) U^*(x + \Lambda_x, y + \Lambda_y) dx dy, \quad (49)$$

and

$$U(x, y) \equiv \frac{E_i(x, y) H_i(x, y)}{E_i(0, 0) H_i(0, 0)}. \quad (50)$$

Now with

$$\Psi(k_x, k_y, \omega) = \hat{Z} \quad (51)$$

and

$$V(k_x, k_y) = \hat{R} \quad (52)$$

we can rewrite Eq. (47) as

$$\sigma_0(\omega) = 16\pi k_0^4 |\zeta(\theta)|^2 \Psi(k_x, k_y, \omega) \cdot V(k_x, k_y) \Big|_{k = (k_B, 0)}, \quad (53)$$

which is discussed in section 3.